The Astrophysical Journal, 947:55 (10pp), 2023 April 20 https://doi.org/10.3847/1538-4357/acc384

© 2023. The Author(s). Published by the American Astronomical Society.
OPEN ACCESS

A Collapsar Origin for GRB 211211A Is (Just Barely) Possible

Jennifer Barnes[1] and Brian D. Metzger[2,3]
[1] Kavli Institute for Theoretical Physics, Kohn Hall, University of California, Santa Barbara, CA 93106, USA; jlbarnes@kitp.ucsb.edu
[2] Department of Physics and Columbia Astrophysics Laboratory, Columbia University, New York, NY 10027, USA
[3] Center for Computational Astrophysics, Flatiron Institute, 162 5th Ave., New York, NY 10010, USA

Received 2022 December 22; revised 2023 March 7; accepted 2023 March 10; published 2023 April 20

Abstract

Gamma-ray bursts (GRBs) have historically been divided into two classes. Short-duration GRBs are associated with binary neutron star mergers (NSMs), while long-duration bursts are connected to a subset of core-collapse supernovae (SNe). GRB 211211A recently made headlines as the first long-duration burst purportedly generated by an NSM. The evidence for an NSM origin was excess optical and near-infrared emission consistent with the kilonova observed after the gravitational-wave-detected NSM GW170817. Kilonovae derive their unique electromagnetic signatures from the properties of the heavy elements synthesized by rapid neutron capture (the *r*-process) following the merger. Recent simulations suggest that the "collapsar" SNe that trigger long GRBs may also produce *r*-process elements. While observations of GRB 211211A and its afterglow rule out an SN typical of those that follow long GRBs, an unusual collapsar could explain both the duration of GRB 211211A and the *r*-process-powered excess in its afterglow. We use semianalytic radiation transport modeling to evaluate low-mass collapsars as the progenitors of GRB 211211A–like events. We compare a suite of collapsar models to the afterglow-subtracted emission that followed GRB 211211A, and find the best agreement for models with high kinetic energies and an unexpected pattern of ^{56}Ni enrichment. We discuss how core-collapse explosions could produce such ejecta, and how distinct our predictions are from those generated by more straightforward kilonova models. We also show that radio observations can distinguish between kilonovae and the more massive collapsar ejecta we consider here.

Unified Astronomy Thesaurus concepts: Gamma-ray bursts (629); Explosive nucleosynthesis (503); Core-collapse supernovae (304); R-process (1324)

1. Introduction

The durations of gamma-ray bursts (GRBs) follow a bimodal distribution, with short (sGRB) and long (lGRB) varieties (Kouveliotou et al. 1993). Observations have tied these two classes of ultrarelativistic jets to distinct progenitors, with lGRBs arising from a subset of highly kinetic core-collapse supernovae (CCSNe; e.g., Galama et al. 1998) and sGRBs originating in compact binary mergers (Abbott et al. 2017).

However, analyses of GRB populations (e.g., Zhang & Choi 2008; Tarnopolski 2015) indicate overlap between the distributions of the durations that characterize each class, raising the specter of GRBs whose timescales are outliers among bursts triggered by the same progenitor (e.g., Bromberg et al. 2013).

While a few lGRBs with no obvious associated supernovae (SNe) have been tentatively attributed to a non-SN progenitor (Gal-Yam et al. 2002; Della Valle et al. 2006; Fynbo et al. 2006), the uncertain nature of the electromagnetic counterparts to compact binary mergers has impeded the definitive association of these bursts with mergers. Nevertheless, it has been suggested that these "hybrid" sGRB/lGRB events are related to a subclass of bursts whose light curves exhibit sGRB-like prompt spikes followed by temporally extended variable X-ray emission lasting tens or hundreds of seconds (e.g., Norris & Bonnell 2006; Perley et al. 2009).

Multimessenger observations of the binary neutron star merger (NSM) GW170817 have improved this situation dramatically by confirming (Goldstein et al. 2017) the theorized (Paczynski 1986; Eichler et al. 1989; Narayan et al. 1992) association between mergers and sGRBs and providing a detailed look at the merger's "kilonova" counterpart (Arcavi et al. 2017; Chornock et al. 2017; Coulter et al. 2017; Drout et al. 2017; Evans et al. 2017; Kasliwal et al. 2017; Kilpatrick et al. 2017; McCully et al. 2017; Nicholl et al. 2017; Shappee et al. 2017; Smartt et al. 2017; Soares-Santos et al. 2017; Tanvir et al. 2017; Valenti et al. 2017).

This allowed Rastinejad et al. (2022) (henceforth R22) to connect the recent GRB 211211A to an NSM (see also Troja et al. 2022) despite its long duration: a T_{90} of ∼34 s according to the Fermi Gamma-ray Burst Monitor (Mangan et al. 2021), or ∼51 s, as measured by Swift's Burst Alert Telescope (Stamatikos et al. 2021). The association was based on the similarity of the optical and near-infrared (NIR) transient that emerged after the burst to the kilonova that arose following GW170817, as well as on the GRB's extended emission, whose duration and spectral evolution mimicked those of the emission observed to follow some sGRBs (e.g., Gompertz et al. 2023).

In a variation of that theme, Yang et al. (2022) proposed that the progenitor of GRB 211211A was the merger of a white dwarf with a neutron star (NS) or stellar-mass black hole (BH), which produces an accretion disk as disrupted white dwarf material circularizes around the central remnant (Fryer & Woosley 1998). However, this interpretation is in tension with semianalytic (Metzger 2012; Margalit & Metzger 2016; Kaltenborn et al. 2022) and numerical (Fernández et al.

Original content from this work may be used under the terms of the Creative Commons Attribution 4.0 licence. Any further distribution of this work must maintain attribution to the author(s) and the title of the work, journal citation and DOI.

2019; Zenati et al. 2019) simulations of these disks, which cast doubt on their ability to effectively neutronize, a precondition for r-production.

The LIGO–Virgo gravitational-wave (GW) detector network was offline at the time of GRB 211211A, so no GW data are available to confirm a compact object merger coincident with the burst. However, the position of the burst, offset by 7.91 kpc from the center of its putative host galaxy (R22), supports the merger theory, as compact object binaries receive kicks during the SN explosions of their component stars, and often travel far from their hosts' centers before they merge (e.g., Kalogera et al. 1998). Some authors (primarily Waxman et al. 2022, who propose an alternate, dust-based explanation for the NIR emission) have cast doubt on the host identification. However, since a distance is required to determine the luminosity of the transient and make comparison to our models, we are unable to engage with the undiscovered-host hypothesis in this work.

Kilonovae are distinguishable by their uniquely red spectra, a hallmark imparted by the high opacities of select elements burned by rapid neutron capture (the r-process), a nucleosynthesis channel that operates in the neutron-rich gas formed from NS material unbound during the merger.

However, kilonovae may not be the only explosions in which the r-process occurs. General relativistic magnetohydrodynamic (GRMHD) simulations of the accretion disks that form in the CCSN explosions of rapidly rotating massive stars ("collapsars") suggest that conditions in these disks can become neutron-rich (Siegel et al. 2019), allowing the r-process to synthesize heavy elements in winds blown off the disk. While not all simulations of collapsar disks predict a robust r-process in disk outflows (Miller et al. 2020; Fujibayashi et al. 2022; Just et al. 2022), the r-process collapsar hypothesis is also supported by patterns in Galactic chemical evolution that seem to require an r-process source that tracks star formation (Côté et al. 2019; Naidu et al. 2022). (A short delay time characterizes CCSNe in general, but is harder to square with NSMs, which represent the endpoint of an evolutionary track that unfolds over hundreds of millions or even billions of years (e.g., Belczynski et al. 2002).)

Collapsars were originally proposed to explain lGRBs and the high-velocity, broad-lined Type Ic (Ic-BL) SNe that often accompany them. The implication then is that r-production may coincide with GRBs regardless of their duration.

We investigate here the possibility that GRB 211211A was triggered by a collapsar, and that its optical and NIR counterpart, which we label as a transient of undetermined classification, T211211A, is the emission from an r-process-enriched SN, albeit a unique one. We describe our semianalytic radiation transport scheme, and the models to which we apply it, in Section 2. In Section 3, we present the models that best reproduce the emission of T211211A, and discuss their properties. We explore in Section 4 what subclass of collapsars might be able to produce these properties, but ultimately fail to convince ourselves that such explosions represent a superior explanation for T211211A. We also outline how radio observations can distinguish between the low-mass collapsar progenitors we focus on and the more conventional kilonova explanation for T211211A. We leave our parting thoughts in Section 5.

2. Methods

We use a semianalytic radiation transport model to predict the emission from r-process-enriched collapsars with a variety of parameters, which we compare to observations of T211211A.

2.1. Radiation Transport Model

We repurpose the radiation transport framework developed by Barnes & Metzger (2022) (hereafter BM22), in which the SN ejecta is divided into concentric shells whose internal energies evolve in response to radioactive heating, adiabatic expansion, and the diffusion and free-streaming of radiation. A full discussion of the implementation can be found in BM22. Here, we highlight minor adjustments we have made to our previous models and methods, which better position us to study the apparently low-mass and high-velocity explosion (R22) that produced T211211A.

First, we no longer assume that ^{56}Ni is evenly distributed in the ejecta. The ejecta configurations we consider are described in more detail in Section 2.2. For consistency, when calculating the gamma-ray opacity to determine the deposition of ^{56}Ni/Co decay energy (à la Colgate et al. 1980), we now include only the ejecta layers that contain ^{56}Ni.

We also now explicitly account for the thermalization of r-process decay products beyond gamma rays. Our current models have lower masses and higher velocities than the r-process-enriched SNe of BM22. The resulting lower densities reduce the optical depth for thermalizing interactions (Barnes et al. 2016), rendering suspect the assumption of efficient thermalization of β^-- and α-particles and fission fragments. We adopt the approximate analytic formula for thermalization efficiency $f_{\rm th}^{rp}$ from Barnes et al. (2016),

$$f_{\rm th}^{rp} = 0.36\left(\exp[-0.55 t_{\rm d}] + \frac{\ln[1 + 0.26 t_{\rm d}^{0.9}]}{0.26 t_{\rm d}^{0.9}}\right),$$

where $t_{\rm d}$ is the time in days, and we have chosen coefficients corresponding to kilonovae with r-process masses and velocities most similar to those of our low-mass collapsar models. This factor is applied to a baseline r-process heating rate $\dot{Q}_{rp} = 2.0 \times 10^{10}\, t_{\rm d}^{-1.3}$ erg s^{-1} g^{-1} (e.g., Metzger et al. 2010; Korobkin et al. 2012).

Finally, the short rise time of T211211A motivates an explicit accounting of the thermal energy deposited in the ejecta during the explosion. (In typical GRB-SNe, which rise to peak $\sim$1–2 weeks after explosion, and which burn larger quantities of ^{56}Ni (Prentice et al. 2016; Taddia et al. 2019; Perley et al. 2020), energy from ^{56}Ni decay rapidly dominates the adiabatically degrading initial thermal energy, preventing the thermal component from influencing the light curve.)

We assume there is a characteristic time, $t_{\rm eq}$, at which the thermal and kinetic energy in a given ejecta layer are in equipartition. The subsequent conversion of the former to the latter accelerates each layer to its final kinetic energy. By the time the SN light curve becomes visible, this conversion is effectively complete; though thermal energy remains, it is insufficient to alter the ejecta's velocity structure. Thus, it is valid to approximate the initial thermal energy as equal to half the final kinetic energy in ejecta shell i, $E_{{\rm k},i}$. The residual

Table 1
Parameters of the Model Suite

Symbol	Definition	Values
$M_{\rm ej}$	Total ejecta mass	$0.5M_\odot$–$1.0M_\odot$, $\Delta M_{\rm ej}/M_{\rm ej} = 0.08$
$v_{\rm ej}$	Average ejecta velocity	$0.1c$–$0.35c$, $\Delta v_{\rm ej}/v_{\rm ej} = 0.18$
M_{56}	^{56}Ni mass	$0.01M_\odot$–$0.1M_\odot$, $\Delta M_{56} = 0.01$
M_{rp}	*R*-process mass	$(0.0, 0.02, 0.05, 0.08)M_\odot$
ψ_{56}	Lowest mass coordinate with ^{56}Ni	0–$(1 - M_{56}/M_{\rm ej})$, $\Delta\psi_{56} = (1 - M_{56}/M_{\rm ej})/5$
ψ_{rp}	Highest mass coordinate with *r*-process matter	$(M_{rp}/M_{\rm ej})$–1, $\Delta\psi_{rp} = (1 - M_{rp}/M_{\rm ej})/5$

energy at t_0, the start time of the simulation, is then

$$E_{{\rm th},i} = \frac{1}{2}E_{{\rm k},i}\left(\frac{t_0}{t_{\rm eq}}\right)^{-1}. \tag{1}$$

The models of R22 also include a thermal component, which they attribute to a cocoon created by the GRB jet as it burrows through the ejecta. In the collapsar scenario, $E_{{\rm th},i}$ could be the product of an initial SN explosion. It could also result from a shock interaction that occurs when the eventual accretion disk wind collides either with the SN ejecta or (in the case of a temporally accelerating disk outflow; see Section 4.1) with itself.

In the interest of limiting the dimensionality of our model suite, we do not treat $t_{\rm eq}$ as a free parameter. However, preliminary explorations have found that $t_{\rm eq} = 1$ s allows us to fit the early blue and ultraviolet emission. This value should be treated as a rough indicator—the exact balance that is achieved between thermal and kinetic energy and whether that balance is uniform over the entire ejecta, for example, are open questions. Nevertheless, it points to heating timescales that could be compatible with either jet breakout or a prompt explosion.

2.2. Model Suite

Our model suite is summarized in Table 1. Based on the arguments of R22, we focus on collapsar models with low masses and high velocities. We consider total ejecta masses in the range $0.5M_\odot \leqslant M_{\rm ej} \leqslant 1.0M_\odot$, and average ejecta velocities $v_{\rm ej}$ of $0.1c$–$0.35c$, where $v_{\rm ej} = \sqrt{2E_{\rm k}/M_{\rm ej}}$, with $E_{\rm k}$ denoting the ejecta's kinetic energy. In all our models, mass density follows a broken power law, $\rho(v) \propto v^{-d}$, with $d = 1$ (10) in the inner (outer) parts of the ejecta. The low luminosities of T211211A, relative to the GRB-SN population, suggest smaller quantities of ^{56}Ni, so we restrict our exploration to models with $0.01M_\odot \leqslant M_{56} \leqslant 0.1M_\odot$.

We consider *r*-process masses $M_{rp}/M_\odot$ of 0.0, 0.02, 0.05, and 0.08. These values are motivated by the luminosity of T211211A, which constrains the total radioactive mass to be low. That they are lower than what was suggested by Siegel et al. (2019) for typical collapsar *r*-process yields ($\lesssim 1M_\odot$) also reflects the overall lower ejecta masses in this work. (Siegel et al. (2019) focused on the more massive progenitors proposed by Heger et al. (2000) to explain CCSNe with higher $M_{\rm ej}$.)

As mentioned in Section 2.1, our ejecta structure is more complex here than in BM22, since the ^{56}Ni mass fraction is no longer required to be uniform. Instead, we extend ^{56}Ni from some inner normalized mass coordinate ψ_{56} to the edge of the ejecta. Such a configuration might be realized if *r*-process winds fail to mix completely with the earlier ejecta containing whatever ^{56}Ni is burned by the prompt explosion. As in BM22, the *r*-process material is mixed from the center of the ejecta out to a normalized mass coordinate ψ_{rp}.

Given $M_{\rm ej}$, M_{56}, and M_{rp}, the quantity ψ_{56} (ψ_{rp}) can take on values from 0 to $[1 - M_{56}/M_{\rm ej}]$ ($M_{rp}/M_{\rm ej}$ to 1). For each parameter combination, we choose five values of ψ_{56} and ψ_{rp} that are spaced uniformly within the ranges defined above. We assume that ^{56}Ni (*r*-process material) is evenly distributed over $m_{\rm enc} \geqslant \psi_{56}$ ($m_{\rm enc} \leqslant \psi_{rp}$), and consider all combinations of ψ_{56} and ψ_{rp} for which the sum of the ^{56}Ni and *r*-process mass fractions is less than or equal to unity everywhere in the ejecta. As in BM22, the opacity of an ejecta shell is determined by its composition. Ejecta lacking both ^{56}Ni and *r*-process elements is assumed to have a baseline opacity of 0.05 cm^2 g^{-1}.

2.3. Model Evaluation

We calculate the broadband evolution of our model in the *ugriz*, *B*, *J*, and *K* bands for every combination of the parameters delineated in Table 1, and compare the results to the afterglow-subtracted photometry of T211211A published in R22, for times $\geqslant$0.05 days.

We quantify the agreement between the data and each instantiation of the model using a simple chi-square metric,

$$\chi^2 = \sum_i \frac{(F_{{\rm obs},i} - F_{{\rm pred},i})^2}{\sigma_i^2} + \sum_j \frac{[\max(F_{{\rm pred},j} - F_{{\rm ul},j},\, 0)]^2}{\sigma_{\rm est}},$$

where $F_{{\rm obs},i}$ ($F_{{\rm pred},i}$) is the observed (predicted) flux corresponding to measurement i, which we derive from reported magnitudes, and σ_i is the uncertainty on the ith measurement. The second sum runs over reported upper limits, $\{F_{{\rm ul},j}\}$. Its terms contribute to χ^2 only when the model's predicted flux exceeds the upper limit. The variable $\sigma_{\rm est}$ is an estimated uncertainty on the upper limit, which we set to 0.1 mag.

3. Results

We perform a grid search to locate the model in the suite with the lowest χ^2, and find that the best match to the data (with $\chi^2 \approx 32$) is achieved by the parameters $M_{\rm ej} = 1.0M_\odot$, $v_{\rm ej} = 0.26c$, $M_{56} = 0.01M_\odot$, $M_{rp} = 0.05M_\odot$, $\psi_{56} = 0.99$, and $\psi_{rp} = 0.76$. The light curve for this model is compared to data in Figure 1.

While this model agrees well with the data, degeneracies among the parameters and the simplicity of the semianalytic model motivate us to investigate additional ejecta models. Furthermore, our procedure does not circumscribe the distribution of ^{56}Ni in the ejecta beyond the physical requirement that $(1 - \psi_{56})M_{\rm ej} \geqslant M_{56}$. The model above, which features an outer shell composed of pure ^{56}Ni, is allowed within our framework. However, it is worth determining whether less extreme ejecta configurations can reproduce the data with comparable fidelity. In Section 3.1, we zoom out and identify larger populations of models with a range of parameters that nonetheless provide good matches to the photometry of T211211A.

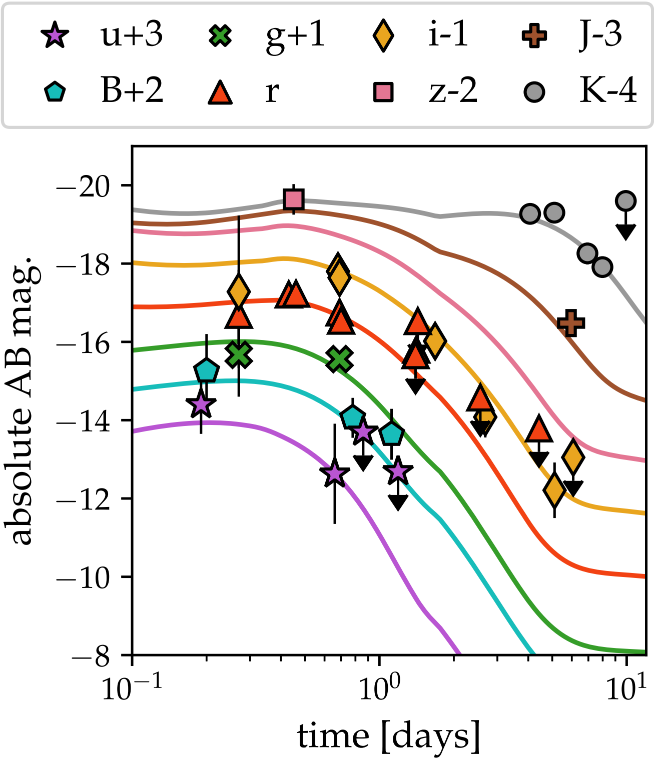

Figure 1. The model from our suite with the lowest χ^2 has $M_{\rm ej} = 1.0 M_\odot$, $v_{\rm ej} = 0.26c$, $M_{56} = 0.01 M_\odot$, $M_{rp} = 0.05 M_\odot$, $\psi_{56} = 0.99$, and $\psi_{rp} = 0.76$. While these parameters provide a good fit to the data, they also define a rather extreme ejecta configuration in which radioactive ^{56}Ni is concentrated in a shell at the outer edge of the ejecta.

3.1. Properties of Successful Models

Before presenting predictions generated by particular parameter combinations, we briefly survey the landscape of all models that provide a satisfactory fit to the observations. We define a satisfactory fit as one for which $\chi^2 \leqslant 100$. Since our model has six degrees of freedom ($N_{\rm dof} = 6$) and is fit against 40 observations and upper limits, this translates to a reduced chi-square metric $\chi^2_{\rm red} \equiv \chi^2 / N_{\rm dof} \lesssim 2.5$. This filter selects ∼1600 models, or just over 2% of the full suite.

Figure 2 shows how the six model parameters are distributed within the good-fitting model set. Models with good fit scores draw from the full range of $M_{\rm ej}$ we consider, though they evince a slight preference for lower ejecta masses. The range of velocities is narrower; agreement with the data is easier to achieve for $v_{\rm ej} \gtrsim 0.2c$. While such velocities are similar to those inferred for the kilonova model of R22, when combined with low-mass collapsars' larger ejecta masses (vis-à-vis kilonovae), they imply kinetic energies near or beyond the upper limit of what has historically been considered possible for SNe (Thompson et al. 2004; Mazzali et al. 2014; Chen et al. 2017).

The parameters governing the *r*-process and ^{56}Ni production and distribution complete the picture. As the third panel shows, all *r*-process masses we consider (except $M_{rp} = 0$, which cannot produce the observed NIR excess) can yield photometry more or less consistent with observations. The masses of ^{56}Ni are more tightly constrained; none of the good-fitting models have $M_{56} > 0.05 M_\odot$. (However, if the distance to GRB 211211A is greater than what was reported in R22, as has been argued by Waxman et al. (2022), somewhat larger quantities of ^{56}Ni may be accommodated.)

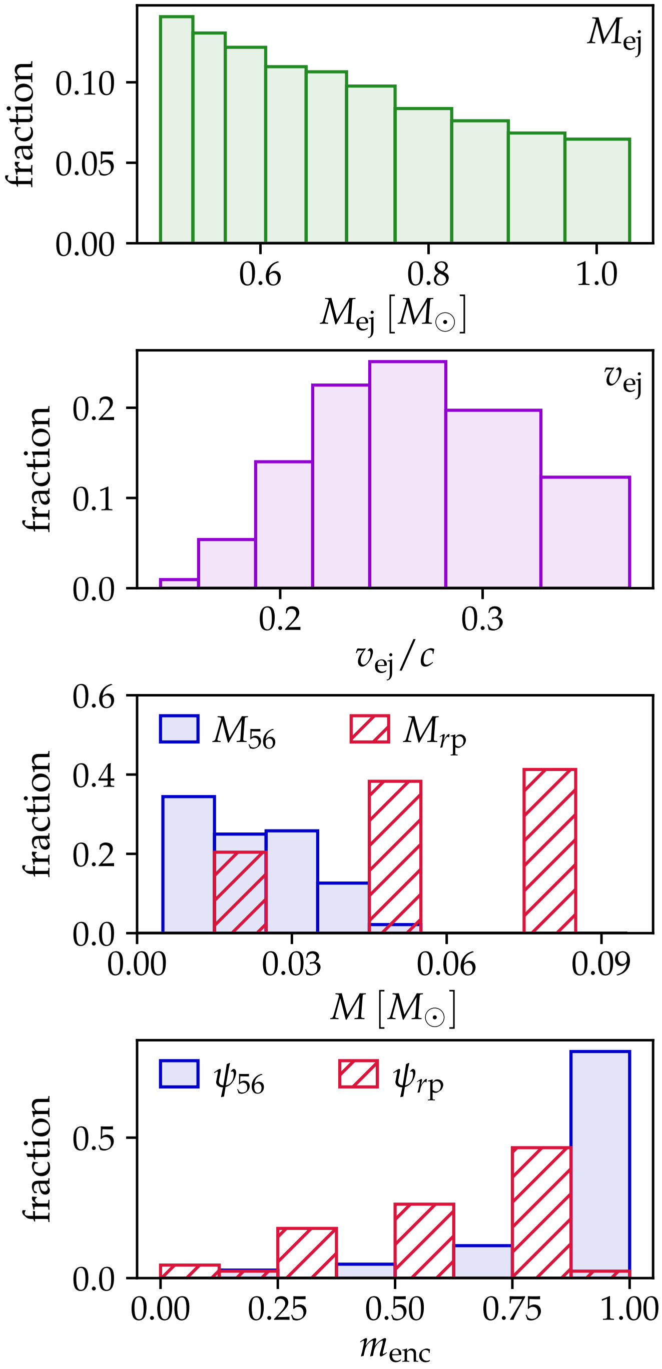

Figure 2. The distribution of parameters for models with $\chi^2 \leqslant 100$. The good-fitting models span the full range of $M_{\rm ej}$ in our model suite (first panel), but draw primarily from the upper end of our $v_{\rm ej}$ range ($v_{\rm ej} \gtrsim 0.2c$; second panel). While various *r*-process masses, $0.01 M_\odot \leqslant M_{rp} \leqslant 0.08 M_\odot$, can be compatible with the observations, lower ^{56}Ni masses ($M_{56} \lesssim 0.05 M_\odot$) are preferred (third panel). The majority of the successful models (fourth panel) feature well-mixed *r*-process material, but concentrate their ^{56}Ni in a thin shell at the outer edge of the ejecta. In the top two panels, the variable widths of the bars reflect the logarithmic spacing of the model parameters.

As indicated in the final panel, the majority of the good-fitting models feature a particular mixing pattern in which *r*-process material is mixed out from the center to fairly high normalized mass coordinates $m_{\rm enc}$, while ^{56}Ni is concentrated in the outermost layers of the ejecta. We will discuss in Section 4 if this configuration is strictly necessary to reproduce the photometry of T211211A, and whether an outflow with

Table 2
Cluster Centroids of the Successful Models

Index (%)	$M_{\rm ej}$[a]	[b]$v_{\rm ej}$	M_{56}[a]	M_{rp}[a]	ψ_{56}	ψ_{rp}
1 (19)	0.61	0.25	0.036	0.053	0.94	0.68
2 (27)	0.65	0.23	0.022	0.067	0.97	0.33
3 (19)	0.60	0.31	0.012	0.053	0.60	0.75
4 (19)	0.88	0.22	0.024	0.053	0.97	0.66
5 (15)	0.63	0.30	0.016	0.049	0.97	0.64

Notes.
[a] Values in units of $M_\odot$.
[b] Values in units of c.

such a radially stratified composition could be produced in nature.

3.2. Successful Model Clusters

To better understand how successful models are situated within the six-dimensional parameter space in which our suite is defined, we use the agglomerative clustering routine of Python's `scikit-learn` package (Pedregosa et al. 2011) to sort them into five groups. The hierarchical clustering algorithm in the `SciPy` library guides our choice of the number of clusters.

The coordinates of the cluster centroids are reported in Table 2, along with the percentage of good-fitting models belonging to each cluster. These data provide additional insight into the combinations of parameters capable of reproducing the photometry of T211211A.

While some of the cluster centroids share the combination of high $E_{\rm k}$ and extreme ψ_{56} suggested by Figure 2, Table 2 shows that these characteristics are not required to reproduce the data within our error tolerance. In fact, aside from centroid 5, all the centroids differ from the best-fit model in at least one significant way. Of particular interest are centroid 1, which has barely half the kinetic energy of the best-fit model; centroid 2, which has both lower $E_{\rm k}$ and lower ψ_{rp}; and centroid 3, which has more extensive ^{56}Ni mixing. Still, however, Table 2 suggests some trade-off between ψ_{56} and $v_{\rm ej}$. Successful models with more extensive ^{56}Ni mixing have higher average velocities. This is required to reproduce the light curves' rapid evolution; a spatially extended emitting region must expand faster to yield a similar light-curve timescale.

In Figure 3, we show the light curves produced by the centroids (1, 2, and 3) highlighted above. While the agreement with observations is by definition poorer than that for the best-fit model, each set of parameters reproduces the fundamental characteristics of T211211A. Given the simplicity of our radiation transport method, the (only slightly) poorer fits are not sufficient reason to discard these models.

4. Discussion

As explained in Section 3.2, due to degeneracies among parameters, low-mass collapsar models with varying physical properties reproduce the photometry of T211211A with comparable fidelity. However, even these degeneracies do not allow infinite flexibility; all of the models have very high velocities and/or poorly mixed ^{56}Ni that would render them outliers among observed GRB-SNe and SNe Ic-BL. We next discuss two possible interpretations of these results, and outline how radio observations can distinguish low-mass collapsars from standard kilonovae.

4.1. A Low-mass Collapsar?

The low ejecta masses we explore here, which are necessitated by the swift evolution of T211211A, are already a departure from the standard collapsar picture, in which a few solar masses of stellar material are ejected (e.g., Cano et al. 2017). The formation of an accretion disk—the defining feature of the collapsar model—is enabled by the rapid rotation of the pre-explosion star. Processes that remove mass from the star earlier in its evolution (e.g., line-driven winds or stripping by a companion) also siphon away the angular momentum that allows disk formation. Our low-$M_{\rm ej}$ models thus correspond more naturally to a scenario in which a large fraction of the pre-explosion mass is captured by the NS or BH formed during the explosion than to one in which the progenitor mass is unusually low at the point of collapse.

The low masses and modest ^{56}Ni production that characterize our good-fitting models could plausibly arise from the explosion of a star with slightly less angular momentum than found in more typical collapsars (e.g., Janiuk & Proga 2008; Murguia-Berthier et al. 2020). The proto-NS produced when such a progenitor collapses (e.g., Dessart et al. 2008) would initially rotate relatively slowly. This, coupled with the delay between the initial collapse and the circularization of the outer layers into an accretion disk, may preclude the kind of prompt ($\lesssim$1 s post-collapse) MHD jetted explosion (e.g., Mösta et al. 2014; Varma et al. 2021) invoked to explain the copious ^{56}Ni production in more typical SNe Ic-BL (e.g., Barnes et al. 2018, though see Zenati et al. 2020 for an alternative ^{56}Ni production site). A weaker explosion could nonetheless launch a low-mass outflow enriched with ^{56}Ni burned in the inner layers (Maeda & Nomoto 2003), thus forming the outer layers of the SN ejecta.

Subsequent material would be ejected once the infalling material had coalesced into an accretion disk. While most of the disk mass would accrete onto the central remnant, powering a relativistic jet (e.g., Bromberg & Tchekhovskoy 2016), a fraction would become gravitationally unbound and expand outward at mildly relativistic velocities (e.g., Siegel & Metzger 2017).

The rate of accretion onto the disk will decline with time, with consequences for nucleosynthesis in the winds. Early high accretion rates through the disk support cooling by neutrino emission (De & Siegel 2021), followed by the neutronization of the disk midplane (Siegel et al. 2019; Fujibayashi et al. 2022; Just et al. 2022). If the newly neutron-rich matter from the midplane escapes the disk without reprotonizing, an r-process can occur as it decompresses upon ejection. As the accretion rate drops, neutronization of the infalling material ceases, truncating r-production in disk outflows. Thereafter, disk winds are composed of He and, to a much lesser degree, iron-peak elements formed in the disk wind outflows when the electron fraction $Y_{\rm e} \approx 0.5$ (Siegel et al. 2019; Zenati et al. 2020). These later ejections account for the nonradioactive mass in our ejecta models.

The time-dependent disk outflow properties are also sensitive to the strength and structure of the magnetic field feeding the BH. The early, r-process-rich winds are likely ejected with velocities $\sim$0.1c, corresponding to a weak poloidal magnetic field (Siegel & Metzger 2017). However, subsequent outflows may be launched at increasingly high velocities, as

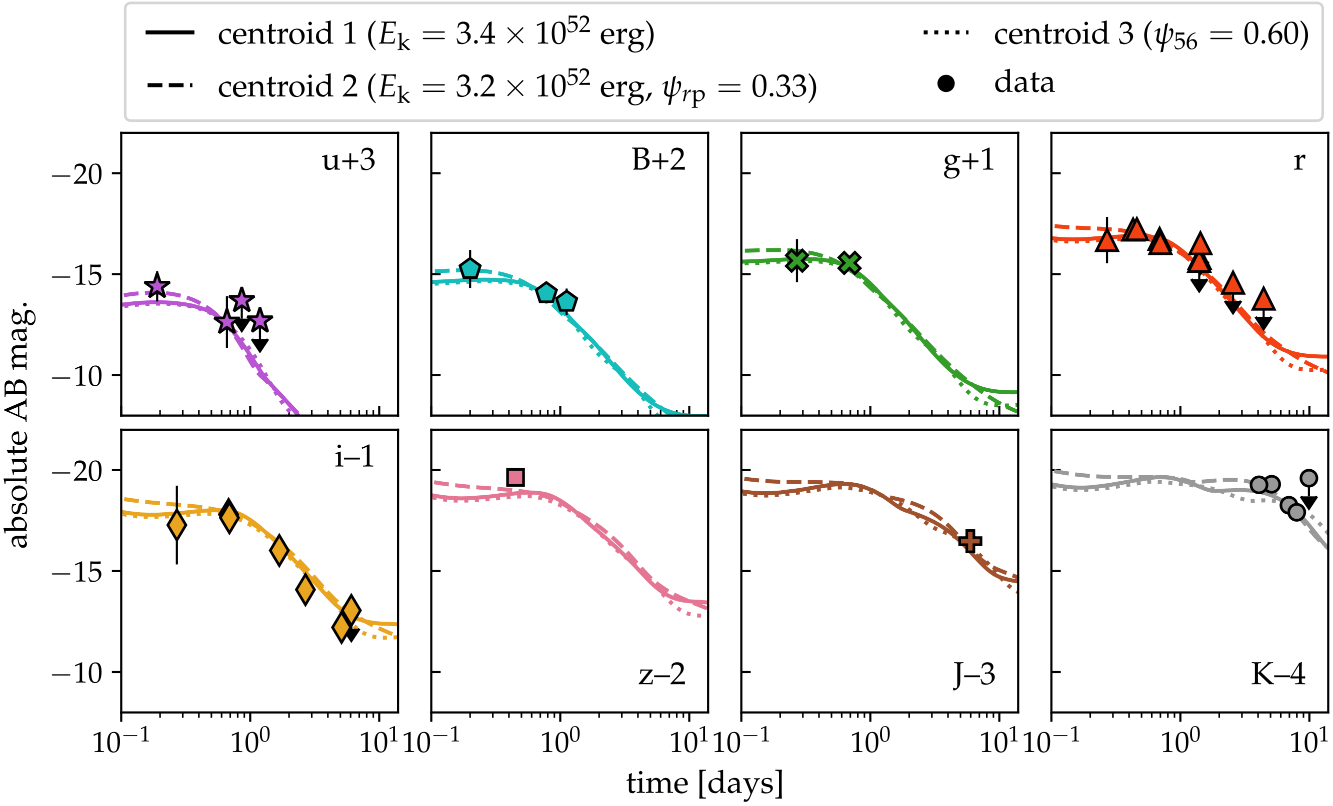

Figure 3. Due to degeneracies among model inputs, diverse sets of parameters produce comparable light curves. The panels above show the broadband light curves for some of the centroids defined in Table 2, which differ from the best-fit model either in their level of ^{56}Ni or *r*-process mixing, or in their kinetic energy. Data from R22 are shown for comparison. While very high E_k and minimal ^{56}Ni mixing are common to many of the good-fitting models, they are apparently not required to reproduce the data.

continual accretion strengthens the magnetic field in the disk (e.g., Tchekhovskoy & Giannios 2015; Gottlieb et al. 2022). For a sufficiently strong and ordered poloidal magnetic flux, wind velocities could reach ≈0.3*c* (Christie et al. 2019).

The higher velocity of the later-stage ejecta would induce mixing between disk wind outflows launched at different times and substantively increase the ejecta's total kinetic energy. Such velocity evolution can therefore account for both the high average velocities and the compositional profiles of the good-fitting models. However, the general lack of evidence for ^{56}Ni mixing means that the earliest mass ejection must occur at velocities high enough to avoid mixing with the disk wind matter.

We see that with a modest degree of fine-tuning, this scenario can explain the fundamental features of our favored ejecta models. We emphasize that this ejecta configuration is likely to differ from that of a garden-variety (higher angular momentum) collapsar, for which the overall ejecta mass is larger and a greater fraction of the disk outflows may be *r*-process-enriched, due to the higher accretion rates at early times.

4.2. *A Collapsar in Kilonova Clothing?*

While we argued in Section 4.1 that nature may produce ejecta similar to those described in Section 3.1, a more skeptical reading of our analysis is that it selects models whose emission is fundamentally similar to that of a kilonova.

The two traits that distinguish our low-mass collapsars from kilonovae are the production, albeit limited, of ^{56}Ni and the significant quantities of non-*r*-process ejecta. However, our good-fitting models have ejecta configurations that dampen the effects of these attributes on their emission, relative to comparable kilonova models.

The low mass of ^{56}Ni, combined with its position at high velocities, limits its impact on the resulting SN. Of the relatively little energy produced by ^{56}Ni decay, only a small fraction is thermalized, due to the low densities near the outer edge of the ejecta, where the ^{56}Ni is located (Colgate et al. 1980). What energy does thermalize diffuses rapidly through the low-optical-depth layers at the ejecta's edge. Its effects are ephemeral, and easily overpowered by the signal from the ejecta's residual thermal energy (Equation (1)).

The relative invisibility of ^{56}Ni in our models is illustrated in the top panel of Figure 4, which shows the impact of removing ^{56}Ni on the light curves of the centroid 3 model (Table 2 and Figure 3). We select centroid 3 because its ^{56}Ni is mixed more thoroughly into the ejecta than that of other centroids, which should increase the sensitivity of the emission to ^{56}Ni decay. Although the model with ^{56}Ni, whose light curves form the upper bounds of the shaded curves in Figure 4's top panel, is brighter than the model without, whose light curves constitute the lower bounds, these differences become most significant at later times, when the data are less constraining, and modeling efforts face more uncertainties (e.g., the nature of optically thin emission; see BM22). The effect at $t \lesssim 1$ day is minimal, because at these times the radiation of residual thermal energy dominates.

To test whether our assumption of an initial thermal component biases our analysis against models with larger

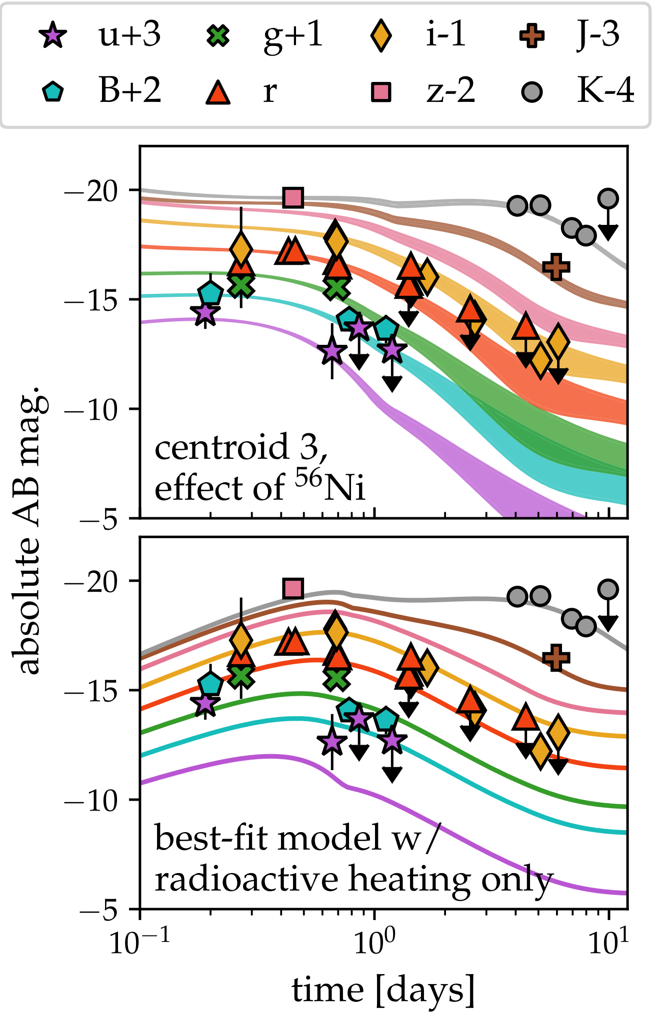

Figure 4. Modified low-mass collapsar models probe the effects of ^{56}Ni on the emission. In both panels, we compare to data from R22. Top panel: Broadband light curves for an unaltered centroid 3 model and a version with $M_{56} = 0$, which form the upper and lower bounds of the filled curves, respectively. Removing ^{56}Ni does not fundamentally change the emission; the apparent differences at $t \gtrsim 1$ day are due mainly to our assumptions about emission from optically thin ejecta. Bottom panel: The best-fit model (with $M_{56} = 0.06 M_{\odot}$ and $\psi_{56} = 0.9$) from a suite in which heating is due solely to radioactivity fails to match the early signal, suggesting that ^{56}Ni heating is not a substitute for $E_{\mathrm{th},i}$. The minor role of ^{56}Ni in our original good-fitting models is not due to our inclusion of an initial thermal energy reservoir (Equation (1)), but instead reflects the incompatibility of the early data with copious, well-mixed ^{56}Ni.

M_{56} or lower ψ_{56}, we run a separate model grid with the same parameter ranges defined in Table 1, but that omits $E_{\mathrm{th},i}$ as defined by Equation (1). Instead, we initialize the internal energies of the ejecta shells by estimating the combined effects of radioactive heating and adiabatic expansion for $t \leqslant t_0$, which results in much lower internal energies.

The bottom panel of Figure 4 shows the light curves of the best-fit model from this grid, which has $M_{\mathrm{ej}} = 0.58 M_{\odot}$, $v_{\mathrm{ej}} = 0.3c$, $M_{56} = 0.06 M_{\odot}$, $M_{rp} = 0.08 M_{\odot}$, $\psi_{56} = 0.90$, and $\psi_{rp} = 0.78$. Its χ^2 is 86, higher than that of the best-fit model in our original suite, but comparable to those of the models in our good-fitting subset. While M_{56} is slightly higher than the ^{56}Ni masses of the original good-fitting model subset (see Figure 2), ^{56}Ni is again concentrated in the ejecta's exterior. This suggests that the ^{56}Ni in our original suite is not forced to the edge of the ejecta by our adopted model for $E_{\mathrm{th},i}$, but rather that significant and/or well-mixed ^{56}Ni decreases agreement with observations. In particular, ^{56}Ni, on its own, cannot explain the earliest emission, particularly in bluer bands. Given that ^{56}Ni is not necessary to explain the late-time signal (see top panel) and appears to be insufficient to explain the earlier parts of the light curves, we conclude that ^{56}Ni is *allowed* but not *required* by the data.

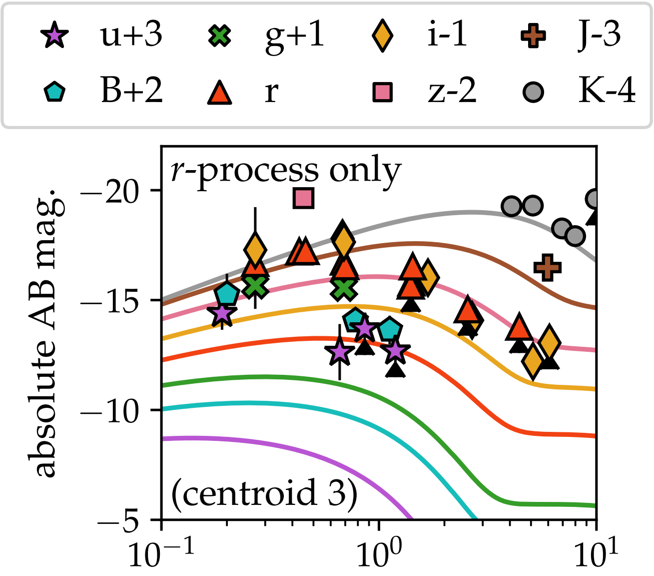

Figure 5. Broadband light curves for a kilonova model containing only the *r*-process ejecta from centroid 3, compared to photometry from R22. Non-*r*-process material is not required to explain the NIR emission of T211211A. However (see text), the lower masses of kilonovae compared to collapsars require different assumptions about the initial thermal energy in order to match the earliest and bluest observations.

The position of ^{56}Ni in our good-fitting models also calls into question the import of the ejecta's nonradioactive material. With ^{56}Ni restricted to the outermost layers, the outward diffusion of the energy from ^{56}Ni decay is effectively independent of M_{ej}. While energy from *r*-process decay must diffuse through a larger fraction of the ejecta, the opacity it encounters is dominated by *r*-process elements; the low opacity of the inert material means its effect on diffusion times is minimal. Thus, though nonradioactive matter dominates M_{ej}, its influence on the emission may be subtle.

To explore the role of nonradioactive material, we transform the centroid 3 collapsar model into a kilonova by excising all of its non-*r*-process ejecta (i.e., this model has $M_{\mathrm{ej}} = M_{rp} = 0.053 M_{\odot}$ and a reduced $v_{\mathrm{ej}} = 0.26c$ on account of its lower mass). Our adopted *r*-process opacity ($\kappa_{rp} = 10$ cm^2 g^{-1}) means this pure *r*-process model corresponds to a kilonova that originated in low-Y_e conditions and is rich in lanthanides and actinides. In other words, its composition is akin to that of a "red" kilonova (e.g., Barnes & Kasen 2013). The model's light curves are displayed in Figure 5.

The agreement in *J* and *K* remains decent, confirming that nonradioactive matter has only a small impact on radiation from the *r*-process-enriched layers. The largest effect is on the early signal, particularly in bluer bands, which suffers because of a reduction in the initial internal energy resulting from the reduced mass of the kilonova ejecta ($E_{\mathrm{th},i}$ scales with shell mass in our model; see Equation (1)).

While we do not attempt to optimize a kilonova model here (see instead R22 or Kunert et al. 2023), our current method for determining $E_{\mathrm{th},i}$ suggests such disagreement would be robust across a broad range of kilonova parameters, owing to the vastly different mass scales of kilonovae and even low-mass collapsars. However, kilonova models with added complexity can avoid the early-time disagreement. R22 achieved a good fit to observations by incorporating two additional, lower-opacity (and hence bluer) kilonova components, as well as a shock-heated cocoon.

In an echo of our earlier discussion of ^{56}Ni, we conclude that large quantities of nonradioactive mass are neither ruled out by the data nor necessary to explain them.

4.3. Tiebreaker: Radio Emission

Our analysis does not conclusively favor a low-mass collapsar origin for T211211A. However, the possibility remains that it, or a future transient with similar properties, could be generated by a collapsar explosion with the combination of parameters detailed in Section 2.2. In the event that nature conspires to produce such an explosion, its late-time radio signal could offer a way to distinguish it from a kilonova born of an NSM.

Both collapsars and kilonovae generate synchrotron radio emission as their ejecta collide with material surrounding the explosion site and decelerate. The rise of the resulting radio light curve, which takes anywhere from a few to several years, is related to the distribution of the fastest material, and therefore sensitive to assumptions about the density profile at the edge of the ejecta. In contrast, the eventual light-curve peak reflects the total kinetic energy contained in the ejecta, which is greater for energetic low-mass collapsars than for mergers by more than an order of magnitude, due principally to the higher masses of the former. Because of the recentness of GRB 211211A, radio nondetections obtained since the burst, like those of R22, most strongly constrain the high-velocity tail of the ejected matter. Continued observations will be invaluable for probing the total kinetic energy of the explosion.

Following Nakar & Piran (2011) and Kathirgamaraju et al. (2019), we estimate the properties of the radio signals from collapsars and kilonovae. The time at which the radio light curve peaks is

$$t_{\mathrm{pk}} \approx 2.7\ \mathrm{yr}\left(\frac{E_{51}}{\beta_0^2}\right)^{1/3}\left(\frac{3}{5\beta_0}-1\right), \qquad (2)$$

where E_{51} is the kinetic energy of the explosion in foe, β_0 is the velocity of the slowest ejecta layer, and we have eliminated the dependence on the circumburst number density by fixing n to the value reported in R22 ($n = 0.54$).

If we additionally adopt the values R22 derived for the fractions of energy in electrons ($\epsilon_e = 3.28 \times 10^{-2}$) and magnetic fields ($\epsilon_B = 1.52 \times 10^{-4}$), we can estimate the peak flux at a given radio frequency ν as

$$F_{\nu,\mathrm{pk}} \approx 26\ \mu\mathrm{Jy}\ E_{51}\beta_0^{\frac{5p-7}{2}}\ \nu_{9.5}^{\frac{1-p}{2}}. \qquad (3)$$

In Equation (3), $\nu_{9.5}$ is ν normalized to $10^{9.5}$ Hz and R22's value of $p = 2.014$ is used to calculate the prefactor (and for consistency should be adopted when evaluating the exponents). We have also converted from luminosity to flux assuming the distance to T211211A is 350 Mpc (R22).

Figure 6 shows the peak time and peak flux at 6 GHz of our best-fit collapsar model and our five centroids, calculated according to Equations (2) and (3) and assuming that $\beta_0 = v_{\mathrm{ej}}/c$ for each model. (The exact value of β_0 is difficult to define for realistic ejecta density profiles, but since the fastest-moving layers of the ejecta carry the majority of the kinetic energy, this choice is reasonable.) The pink shaded region in Figure 6 shows the range of peak properties for collapsars with parameters that this work suggests might produce emission consistent with T211211A: $0.5M_\odot \leqslant M_{\mathrm{ej}} \leqslant 1.0M_\odot$ and $0.2c \leqslant v_{\mathrm{ej}} \leqslant 0.35c$.

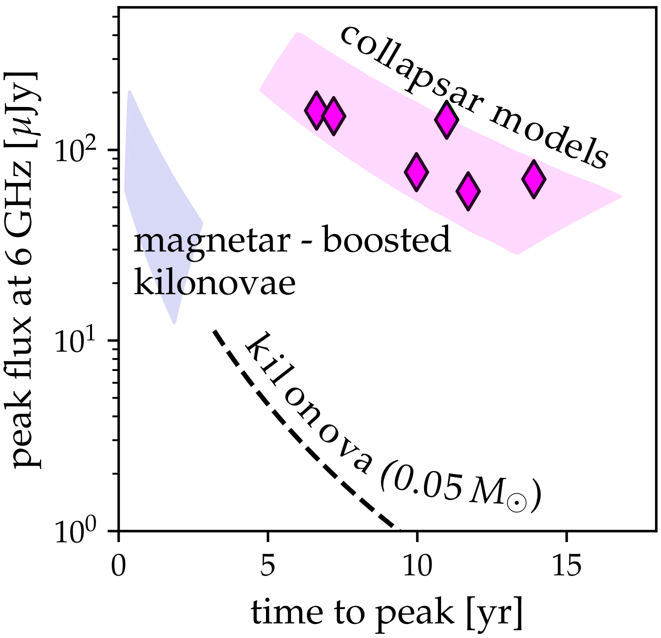

Figure 6. The radio afterglows of low-mass collapsars occupy a region of parameter space distinct from those of kilonovae. The time-to-peak and peak flux at 6 GHz for our best-fit collapsar model and the centroid parameters of Table 2 are plotted as pink diamonds. The pink shaded region shows the expected peak properties for collapsars with masses (velocities) in the range $0.5M_\odot$–$1.0M_\odot$ ($0.2c$–$0.35c$), which typify the properties of our good-fitting models. We show as a dashed black line the peak properties of kilonovae with $m_{\mathrm{ej,k}} = 0.05M_\odot$ and $0.1c \leqslant v_{\mathrm{ej,k}} \leqslant 0.3c$. The radio signal from a kilonova whose ejecta is accelerated by spin-down energy from a long-lived magnetar can have brightness comparable to that of collapsar models, but peaks on a much faster timescale. The blue shaded region, corresponding to $0.03M_\odot \leqslant m_{\mathrm{ej,k}} \leqslant 0.1M_\odot$ and $0.35c \leqslant v_{\mathrm{ej,k}} \leqslant 0.55c$, indicates the expected peak properties of the radio light curve from such "boosted" kilonovae.

For comparison, we also plot the peak properties for two classes of kilonovae. For the first, standard case, we consider a kilonova ejecta of mass $m_{\mathrm{ej,k}} = 0.05M_\odot$ (the total r-process mass suggested by R22) and a range of velocities $0.1c \leqslant v_{\mathrm{ej,k}} \leqslant 0.3c$. (We consider a range of velocities because the minimum velocity is nontrivial to define for a multi-component model like the one constructed in R22.) The resulting peak fluxes and timescales are plotted as a dashed black line. Due to their greater kinetic energies, the collapsar models have much higher fluxes at peak than a standard kilonova would have when the parameters beyond E_{51} and β_0 are held constant.

A second, as-yet-unobserved class of kilonovae could result from a merger that forms a long-lived, rapidly rotating magnetar. Before collapsing to a BH, such a magnetar would transfer much of its rotational energy to the ejecta from the merger, thereby producing an extremely high-velocity outflow (Metzger & Bower 2014; Schroeder et al. 2020). (In fact, building on Metzger et al. (2008), R22 invoked an initially stable magnetar to explain the anomalously long duration of the gamma-ray emission from GRB 211211A.)

The energy transferred to the kilonova ejecta during magnetar spin-down would likely be $E_{\rm rot} \gtrsim 10^{52}$ erg (e.g., Bucciantini et al. 2012). For typical $m_{\rm ej,k}$ (∼a few hundredths of a solar mass), this produces velocities $v_{\rm ej,k} \sim 0.5c$, higher than what is expected for either the collapsar or the standard kilonova case (and higher than the collapsar and kilonova velocities favored by this work and R22, respectively).

By the scaling laws of Equations (2) and (3), the synchrotron emission from a kilonova accelerated by magnetar spin-down would be significantly brighter than that from a standard kilonova, and would peak much sooner than that from either a standard kilonova or a collapsar. We indicate the range of peak radio properties expected for such a scenario by the blue shaded region in Figure 6, though we note that a substantial injection of spin-down energy by a long-lived magnetar would be difficult to reconcile with the optical and NIR light curves of T211211A.

Ground-based radio telescopes (e.g., the Very Large Array) could easily distinguish among these cases with long-term monitoring of the radio signal.

5. Conclusion

We have used semianalytic radiation transport modeling to investigate the possibility that the ambiguous GRB 211211A originated not in a compact object merger, as proposed by R22, Troja et al. (2022), and Yang et al. (2022), but rather in the CCSN explosion of a star with less angular momentum than that of a typical lGRB progenitor. According to this theory, the *r*-process elements that provide the NIR excess observed in the GRB afterglow were synthesized not from neutron-rich material expelled during the coalescence of an NS binary, but from ordinary stellar material that became neutron-rich in an accretion disk midplane as a result of weak interactions in the presence of electron degeneracy (Siegel et al. 2019). Our model assumes that the expulsion of this material from the disk enriches the central core of the SN ejecta with *r*-process elements.

We find that certain regions of our parameter space produce emission that broadly agrees with observations of the afterglow-subtracted light curves of T211211A. However, the particular constellation of parameters required to achieve a reasonable fit—namely very high velocities and the presence of ^{56}Ni only at the outer edges of the ejecta—points to an explosion distinct from the standard picture of collapsars.

Further bedeviling the interpretation of T211211A is the fact that ^{56}Ni—at least when restricted to the ejecta's edge—has only a minor impact on the emission. The large quantity of nonradioactive material (the other feature that distinguishes our low-mass collapsars from the merger-driven models of R22 and Yang et al. 2022) plays a larger role, but its importance is contingent on our assumptions about how internal energy is generated in the earliest phases of the explosion. Equally plausible treatments put forward by R22 are able to account for the early blue emission without appealing to mass beyond the *r*-process material required to explain the NIR excess. Thus we conclude that although a collapsar could explain T211211A, nothing about T211211A's emission serves as a smoking gun for a collapsar progenitor.

Fortunately, the lack of clarity surrounding GRB 211211A and its afterglow will itself be transient. We have shown that radio observations can easily distinguish signals produced by collapsar ejecta from those generated by the much less massive outflows produced by merging compact objects. Furthermore, in the future, GW detectors will definitively settle the question of a merger or collapsar trigger for difficult-to-classify GRBs. In the multimessenger era, we can hope to understand the full diversity of GRB emission and progenitors.

The authors thank A. Polin, J. Rastinejad, G. Schroeder, and A.V. Villar for helpful conversations, and the anonymous reviewer for suggestions that helped us improve the manuscript. J.B. gratefully acknowledges support from the Gordon and Betty Moore Foundation through grant No. GBMF5076. B.D.M. is supported in part by the National Science Foundation (grant Nos. AST-2009255 and AST-2002577). This work was performed in part at the Aspen Center for Physics, which is supported by National Science Foundation grant No. PHY-1607611, as well as at the Kavli Institute for Theoretical Physics at the University of California at Santa Barbara, which receives funding from the National Science Foundation though grant No. PHY-1748958.

ORCID iDs

Jennifer Barnes https://orcid.org/0000-0003-3340-4784
Brian D. Metzger https://orcid.org/0000-0002-4670-7509

References

Abbott, B. P., Abbott, R., Abbott, T. D., et al. 2017, ApJL, 848, L13
Arcavi, I., Hosseinzadeh, G., Howell, D. A., et al. 2017, Natur, 551, 64
Barnes, J., Duffell, P. C., Liu, Y., et al. 2018, ApJ, 860, 38
Barnes, J., & Kasen, D. 2013, ApJ, 775, 18
Barnes, J., Kasen, D., Wu, M.-R., & Martínez-Pinedo, G. 2016, ApJ, 829, 110
Barnes, J., & Metzger, B. D. 2022, ApJL, 939, L29
Belczynski, K., Kalogera, V., & Bulik, T. 2002, ApJ, 572, 407
Bromberg, O., Nakar, E., Piran, T., & Sari, R. 2013, ApJ, 764, 179
Bromberg, O., & Tchekhovskoy, A. 2016, MNRAS, 456, 1739
Bucciantini, N., Metzger, B. D., Thompson, T. A., & Quataert, E. 2012, MNRAS, 419, 1537
Cano, Z., Wang, S.-Q., Dai, Z.-G., & Wu, X.-F. 2017, AdAst, 2017, 8929054
Chen, K.-J., Moriya, T. J., Woosley, S., et al. 2017, ApJ, 839, 85
Chornock, R., Berger, E., Kasen, D., et al. 2017, ApJL, 848, L19
Christie, I. M., Lalakos, A., Tchekhovskoy, A., et al. 2019, MNRAS, 490, 4811
Colgate, S. A., Petschek, A. G., & Kriese, J. T. 1980, ApJL, 237, L81
Côté, B., Eichler, M., Arcones, A., et al. 2019, ApJ, 875, 106
Coulter, D. A., Foley, R. J., Kilpatrick, C. D., et al. 2017, Sci, 358, 1556
De, S., & Siegel, D. M. 2021, ApJ, 921, 94
Della Valle, M., Chincarini, G., Panagia, N., et al. 2006, Natur, 444, 1050
Dessart, L., Burrows, A., Livne, E., & Ott, C. D. 2008, ApJL, 673, L43
Drout, M. R., Piro, A. L., Shappee, B. J., et al. 2017, Sci, 358, 1570
Eichler, D., Livio, M., Piran, T., & Schramm, D. N. 1989, Natur, 340, 126
Evans, P. A., Cenko, S. B., Kennea, J. A., et al. 2017, Sci, 358, 1565
Fernández, R., Margalit, B., & Metzger, B. D. 2019, MNRAS, 488, 259
Fryer, C. L., & Woosley, S. E. 1998, ApJL, 502, L9
Fujibayashi, S., Sekiguchi, Y., Shibata, M., & Wanajo, S. 2022, arXiv:2212.03958
Fynbo, J. P. U., Watson, D., Thöne, C. C., et al. 2006, Natur, 444, 1047
Galama, T. J., Vreeswijk, P. M., van Paradijs, J., et al. 1998, Natur, 395, 670
Gal-Yam, A., Ofek, E. O., & Shemmer, O. 2002, MNRAS, 332, L73
Goldstein, A., Veres, P., Burns, E., et al. 2017, ApJL, 848, L14
Gompertz, B. P., Ravasio, M. E., Nicholl, M., et al. 2023, NatAs, 7, 67
Gottlieb, O., Liska, M., Tchekhovskoy, A., et al. 2022, ApJL, 933, L9
Heger, A., Langer, N., & Woosley, S. E. 2000, ApJ, 528, 368
Janiuk, A., & Proga, D. 2008, ApJ, 675, 519
Just, O., Goriely, S., Janka, H. T., Nagataki, S., & Bauswein, A. 2022, MNRAS, 509, 1377
Kalogera, V., Kolb, U., & King, A. R. 1998, ApJ, 504, 967
Kaltenborn, M. A., Fryer, C. L., Wollaeger, R. T., et al. 2022, arXiv:2209.13061

Kasliwal, M. M., Nakar, E., Singer, L. P., et al. 2017, Sci, 358, 1559
Kathirgamaraju, A., Giannios, D., & Beniamini, P. 2019, MNRAS, 487, 3914
Kilpatrick, C. D., Foley, R. J., Kasen, D., et al. 2017, Sci, 358, 1583
Korobkin, O., Rosswog, S., Arcones, A., & Winteler, C. 2012, MNRAS, 426, 1940
Kouveliotou, C., Meegan, C. A., Fishman, G. J., et al. 1993, ApJL, 413, L101
Kunert, N., Antier, S., Nedora, V., et al. 2023, arXiv:2301.02049
Maeda, K., & Nomoto, K. 2003, NuPhA, 718, 167
Mangan, J., Dunwoody, R., Meegan, C. & Fermi GBM Team 2021, GCN, 31210, 1
Margalit, B., & Metzger, B. D. 2016, MNRAS, 461, 1154
Mazzali, P. A., McFadyen, A. I., Woosley, S. E., Pian, E., & Tanaka, M. 2014, MNRAS, 443, 67
McCully, C., Hiramatsu, D., Howell, D. A., et al. 2017, ApJL, 848, L32
Metzger, B. D. 2012, MNRAS, 419, 827
Metzger, B. D., & Bower, G. C. 2014, MNRAS, 437, 1821
Metzger, B. D., Martínez-Pinedo, G., Darbha, S., et al. 2010, MNRAS, 406, 2650
Metzger, B. D., Quataert, E., & Thompson, T. A. 2008, MNRAS, 385, 1455
Miller, J. M., Sprouse, T. M., Fryer, C. L., et al. 2020, ApJ, 902, 66
Mösta, P., Richers, S., Ott, C. D., et al. 2014, ApJL, 785, L29
Murguia-Berthier, A., Batta, A., Janiuk, A., et al. 2020, ApJL, 901, L24
Naidu, R. P., Ji, A. P., Conroy, C., et al. 2022, ApJL, 926, L36
Nakar, E., & Piran, T. 2011, Natur, 478, 82
Narayan, R., Paczynski, B., & Piran, T. 1992, ApJL, 395, L83
Nicholl, M., Berger, E., Kasen, D., et al. 2017, ApJL, 848, L18
Norris, J. P., & Bonnell, J. T. 2006, ApJ, 643, 266
Paczynski, B. 1986, ApJL, 308, L43
Pedregosa, F., Varoquaux, G., Gramfort, A., et al. 2011, J. Mach. Learn. Res., 12, 2825
Perley, D. A., Fremling, C., Sollerman, J., et al. 2020, ApJ, 904, 35
Perley, D. A., Metzger, B. D., Granot, J., et al. 2009, ApJ, 696, 1871
Prentice, S. J., Mazzali, P. A., Pian, E., et al. 2016, MNRAS, 458, 2973
Rastinejad, J. C., Gompertz, B. P., Levan, A. J., et al. 2022, Natur, 612, 223
Schroeder, G., Margalit, B., Fong, W.-f., et al. 2020, ApJ, 902, 82
Shappee, B. J., Simon, J. D., Drout, M. R., et al. 2017, Sci, 358, 1574
Siegel, D. M., Barnes, J., & Metzger, B. D. 2019, Natur, 569, 241
Siegel, D. M., & Metzger, B. D. 2017, PhRvL, 119, 231102
Smartt, S. J., Chen, T. W., Jerkstrand, A., et al. 2017, Natur, 551, 75
Soares-Santos, M., Holz, D. E., Annis, J. & Dark Energy Survey,& Dark Energy Camera GW-EM Collaboration 2017, ApJL, 848, L16
Stamatikos, M., Barthelmy, S. D., D'Ai, A., et al. 2021, GCN, 31209, 1
Taddia, F., Sollerman, J., Fremling, C., et al. 2019, A&A, 621, A71
Tanvir, N. R., Levan, A. J., González-Fernández, C., et al. 2017, ApJL, 848, L27
Tarnopolski, M. 2015, A&A, 581, A29
Tchekhovskoy, A., & Giannios, D. 2015, MNRAS, 447, 327
Thompson, T. A., Chang, P., & Quataert, E. 2004, ApJ, 611, 380
Troja, E., Fryer, C. L., O'Connor, B., et al. 2022, Natur, 612, 228
Valenti, S., Sand, D. J., Yang, S., et al. 2017, ApJL, 848, L24
Varma, V., Müller, B., & Obergaulinger, M. 2021, MNRAS, 508, 6033
Waxman, E., Ofek, E. O., & Kushnir, D. 2022, arXiv:2206.10710
Yang, J., Ai, S., Zhang, B.-B., et al. 2022, Natur, 612, 232
Zenati, Y., Perets, H. B., & Toonen, S. 2019, MNRAS, 486, 1805
Zenati, Y., Siegel, D. M., Metzger, B. D., & Perets, H. B. 2020, MNRAS, 499, 4097
Zhang, Z. B., & Choi, C. S. 2008, A&A, 484, 293